Journal of The Electrochemical Society, **159** (3) B315-B323 (2012)
0013-4651/2012/159(3)/B315/9/$28.00 © The Electrochemical Society

Three-Dimensional Simulation of SOFC Anode Polarization Characteristics Based on Sub-Grid Scale Modeling of Microstructure

Masashi Kishimoto,[z] Hiroshi Iwai, Motohiro Saito, and Hideo Yoshida

Department of Aeronautics and Astronautics, Kyoto University, Yoshida Honmachi, Sakyo-ku, Kyoto 606-8501, Japan

Three-dimensional numerical analysis of solid oxide fuel cell (SOFC) anode polarization is conducted with a microstructure obtained by a focused ion beam and scanning electron microscope (FIB-SEM). Electronic, ionic and gaseous transports with electrochemical reaction are considered in the porous anode. A sub-grid scale (SGS) model is newly developed and effectively used to consider the structural information whose characteristic scale is smaller than calculation grid size. The proposed SGS models are designed to keep the quality of the structural information which is inevitably lost by resampling process in grid generation. Through comparisons between the simulation results and the experimental data, it was found that the SGS model can either improve the simulation accuracy under a given calculation grid system or reduce computational load for the same degree of simulation accuracy.
 [DOI: 10.1149/2.086203jes]

Manuscript submitted September 19, 2011; revised manuscript received December 16, 2011. Published January 10, 2012. This was Paper 977 presented at the Montreal, QC, Canada, Meeting of the Society, May 1–6, 2011.

Solid oxide fuel cell (SOFC) has been receiving attentions as one of the most promising power generation systems owing to its high efficiency and fuel flexibility. Since the performance of SOFCs largely depends on the microstructure of porous electrodes, it is important to find the relationships between the electrode microstructure and performance to improve SOFC electrodes. A focused ion beam and scanning electron microscope (FIB-SEM) technique is a powerful mean to directly observe the 3D microstructure of SOFC electrodes.[1–4] From the obtained 3D structure, we can quantitatively evaluate many microstructural parameters which directly affect electrode performance.

As an application of the valuable data obtained by the FIB-SEM, development of a reliable simulation model to predict the electrode performance is strongly required to clarify the effects of the microstructure on the performance. We[5] recently conducted a 1D numerical simulation and predicted the anode polarization characteristics; microstructural parameters obtained from a FIB-SEM dataset were applied in the simulation. In the 1D approach, however, some of the structural information, such as structural non-uniformity, is inevitably neglected. On the other hand, 3D simulations are capable of providing detailed information of the complex phenomena in the porous electrodes. Shikazono et al.[6] applied lattice Boltzmann method (LBM) to predict the anode polarization characteristics using 3D microstructure obtained by FIB-SEM. Also, Shearing et al.[7] applied volume of fluid (VOF) method for the similar purpose. Simulation in this direction is expected to become a powerful tool in the research of porous electrode.

For a grid system of the 3D simulation, a direct application of the image voxel of the FIB-SEM observation (length scale ∼30 nm) may be possible. However, it is a common practice today to resample the original FIB-SEM dataset to make a calculation grid system, structured or unstructured, to reduce the computational load within a realistic limit. The resampling process, however, raises a question whether the resampled dataset is still a good representation of the original microstructure because it often results in lower spatial resolution[6,7] and the structure smaller than the calculation grid size (sub-grid information) may be lost. It may even cause an artificial change of the microstructure. If we consider the rapid development of FIB-SEM technique and our boundless desire for a high resolution and a large observation volume, direct calculation using the image voxel as simulation grid will not always be available. In order to take the best advantage of the precious 3D image dataset obtained by FIB-SEM observation, development of a proper and efficient resampling process is required.

In this study, we newly introduce a sub-grid scale (SGS) model, in which the information of the microstructures, whose characteristic scale is smaller than the grid size, are considered within each grid. Specifically, in the SGS model, not only the volume conservation of each porous component is locally satisfied, but also higher-order quantities associated with the structural inhomogeneity is evaluated. We investigate the effect of the proposed SGS models in the numerical analysis, and validate their applicabilities.

Experimental

Cell preparation and electrochemical characterization.— In this study, we examine the Ni-YSZ cermet anode (Ni:YSZ = 50:50 vol. %, YSZ: 8mol %Y_2O_3 – ZrO_2) of a button cell. A disk of 8 mol % YSZ (yttria-stabilized zirconia, Tosoh Co., 20 mm diameter, 500 μm thickness) is used as an electrolyte. NiO powder (Wako Pure Chemical Industries, Ltd.) and YSZ powder (Tosoh Co.) are mixed and ball-milled for 24 h with ethanol and zirconia balls (ϕ4.0 mm) to disperse the particles. After the milling, ethanol is evaporated using a hot stirrer at 100°C, and the resultant powder is pre-sintered at 1400°C for 5 h. After that it is grinned for 3 h and mixed with polyethylene glycol to form slurry. Finally, the anode slurry is screen-printed on the YSZ electrolyte and sintered at 1400°C for 5 h. The $(La_{0.8}Sr_{0.2})_{0.97}MnO_3$ (LSM) is used as a cathode material, which is prepared from corresponding metal acetates. First, all reagents are dissolved together in water considering the required molar ratio of metals. Next water is evaporated at about 120°C, and the resultant powder is ball-milled for 24 h with zirconia balls (ϕ10 mm). The resultant powder is calcined at 900°C for 10 h, and mixed with polyethylene glycol to form slurry. Finally, the cathode slurry is screen-printed on the other face of the electrolyte and sintered at 1150°C for 5 h. A platinum reference electrode is attached around the side edge of the thin electrolyte disk.

The electrochemical characterization of the cell is conducted as follows. First, the cell is sandwiched by alumina tubes with Pyrex glass seal as shown in Fig. 1 and heated up to the testing temperature by an electric furnace. Second, NiO–YSZ is reduced under pure hydrogen atmosphere at 1000°C for 1 h. Third, the power generation with potentiostatic load is conducted for 3 h at the terminal voltage 0.7 V to stabilize the initial performance. Feeding gas is 3 % H_2O – 97 % H_2 and air (79 % N_2 – 21 % O_2) to anode and cathode, respectively. A total gas flow rates are 100 mL min^{-1} at both electrode sides. The fuel mixture is prepared by bubbling H_2 through water. Finally, under the various fuel conditions (x % H_2O – 100–x % H_2, x = 1.2, 3.0, 10), current-voltage characteristics and AC impedance measurements are conducted between anode and reference electrode at 1000°C using the Solatron 1287 electrochemical interface and

[z] E-mail: kishimoto.masashi.67w@st.kyoto-u.ac.jp

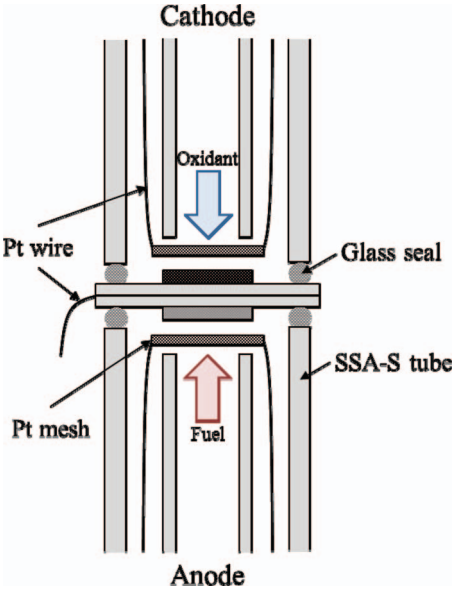

Figure 1. Schematic picture of the experimental setup.

Solatron 1255 frequency analyzer. The applied frequency is in the range of 0.1 Hz to 1 MHz with the voltage amplitude of 10 mV.

FIB-SEM imaging.— After the electrochemical characterization, the cell is cooled down in reductive atmosphere. The porous anode is infiltrated with epoxy resin (Marumoto Struers KK) under vacuum condition so that the pores of the electrode can be easily distinguished in SEM observation. The cured sample is polished using an Ar-ion beam cross-section polisher (JEOL Ltd., SM-09010) and provided to the FIB-SEM observation.

The 3D microstructure of the Ni-YSZ anode is observed by the FIB-SEM system. The FIB-SEM system, NVision 40, is equipped with a Gemini FE-SEM column (Zeiss), a zeta FIB column (SIINT) and a multichannel gas injection system (SIINT). An in-lens secondary electron detector is used for the microstructural observation with an acceleration voltage around 1 to 2 kV. Figure 2a shows an example of the obtained cross-sectional images. In the images, white, gray and black part corresponds to Ni, YSZ and pore phase, respectively. The set of the cross-sectional images obtained by the FIB-SEM tends to have misalignment between the images. Therefore, we put lines on the sample surface before the observation and use them for an alignment mark.

We extract regions available for the later analysis and conduct the phase separation based on the image brightness. After the alignment and the phase separation, the sequential set of 2D images is lined up with the actual increment in the FIB-SEM observation and the 3D porous microstructure is reconstructed in a virtual field. Figure 2b shows the reconstructed microstructure of the porous anode. We use the commercial image processing software, Avizo (Mercury Computer Systems, Inc.), for the phase separation, 3D reconstruction, and some of the quantification explained afterward. In this study, orthogonal coordinate axes X and Y are embedded on a 2D SEM image and Z is the proceeding direction of the FIB milling.

Numerical Model

We conduct a numerical simulation of anode polarization characteristics with 3D porous structure obtained by the FIB-SEM. The simulation is based on finite volume method (FVM) with a structured hexahedral grid system. Figure 3 shows the schematic picture of the calculation domain. The anode thickness of the cell used in the experiment was approximately 30 μm. Therefore, the whole anode structure obtained by the FIB-SEM is mirror-symmetrically extended in the Z direction 5 times to equivalently attain the thickness. We consider the conservation of electrons in Ni phase, oxygen ions in YSZ phase and gas species in pore phase and also electrochemical oxidation of hydrogen at three-phase boundary (TPB). Temperature and total gas pressure are assumed to be constant and uniform over the whole anode region.

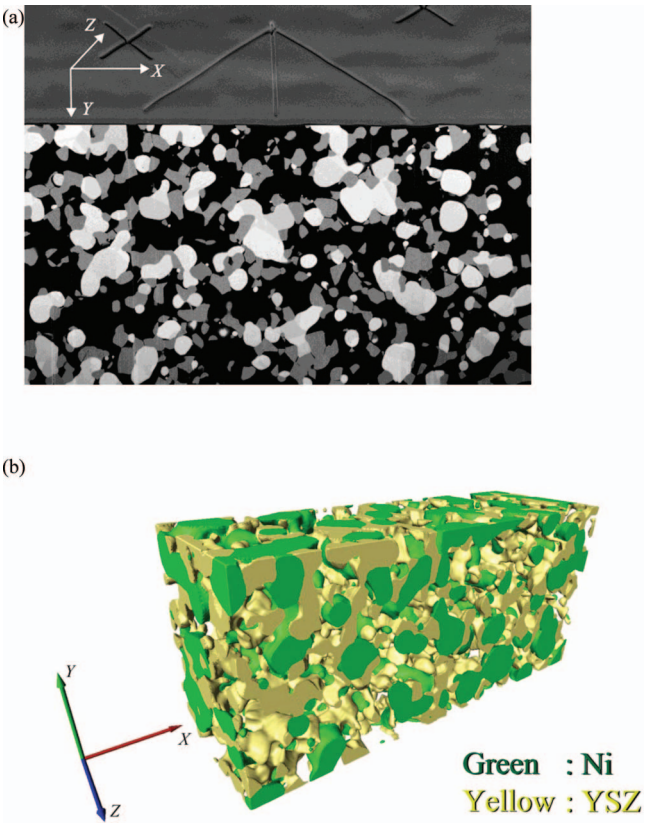

Figure 2. FIB-SEM observation of the SOFC porous anode. (a) Example of the cross-sectional images. (b) Reconstructed 3D structure (Green:Ni, Yellow:YSZ).

In FVM, LBM, VOF and many other simulation methods, the physical space in the computational domain is divided into a number of small volumes (grids) to be used as a grid system. Although it is ideal if the image voxel of the FIB-SEM observation is directly used as the grid system, it is often generated by resampling the FIB-SEM data in practice. After the resampling process, the size of the generated grids

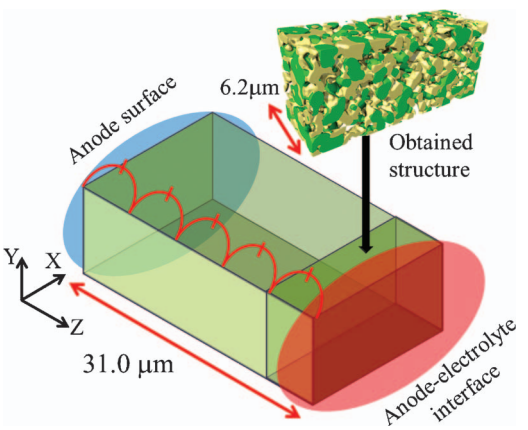

Figure 3. Schematic picture of the calculation domain.

is larger than that of the image voxels. Reduction of computational load by limiting the number of grids is the main reason to perform the resampling. The resampling is also necessary when the computational methods like LBM are employed; this is because they require the computation grid to have a cubic form while the image voxel of the FIB-SEM observation is generally non-cubic. Since the size of the grids is larger than the image voxel of the FIB-SEM observation, each grid potentially contains maximum three phases and their distributions inside the grid are associated with the original microstructure. In a simple resampling process, the microstructure within a grid is neglected and the grid is often replaced by the phase of the largest volume fraction in the grid. Therefore, as far as the resampling procedure is involved, the structural information whose characteristic scale is smaller than grid size is lost, which has negative effects on the accuracy of the simulation. To solve this problem, we propose to use a model, which considers the sub-gird-scale information of porous structure in the calculation domain and reduces the loss of the quality of the structural information. In this study, we introduce the following two simple SGS models and investigate the effects on the numerical analysis.

SGS model 1: Volume conservation.— As the simplest SGS model, we consider the conservation of the phase volume in each calculation grid. Schematic picture of the model concept is shown in Fig. 4a. The numbers of voxels corresponding to Ni, YSZ and pore phases are counted and volume fractions are obtained in each grid. By using the volume fractions, effective transport coefficients, Γ_l^{eff}, are evaluated in each grid as follows:

$$\Gamma_l^{eff} = V_l \Gamma_l \quad [1]$$

where Γ_l is the bulk transport coefficient and V_l is the volume fraction of phase l. In this study, Γ_l corresponds to electron conductivity in Ni phase (σ_{el}), oxygen ion conductivity in YSZ phase (σ_{io}) or gas diffusivity in pore phase (D_{ij}, D_K). In a finite volume method, any transport between neighboring two grids proceeds through the interface they share. As the effective transport coefficients, Γ_l, of the two grids are generally different, an averaged effective transport coefficient between the two grids needs to be evaluated to calculate the transport flux through the interface. Since the equally spaced grid system is used in this study, it is evaluated as harmonic average of the effective transport coefficients of the neighboring two grids. Following formula shows the averaged effective transport coefficient between grid (i, j, k) and grid ($i + 1$, j, k).

$$\Gamma^{eff}_{l,(i+\frac{1}{2},j,k)} = \left(\frac{1}{\Gamma^{eff}_{l,(i,j,k)}} + \frac{1}{\Gamma^{eff}_{l,(i+1,j,k)}} \right)^{-1} \quad [2]$$

Note that the LHS of eq. 2 is defined at the location of $i + 1/2$, which corresponds to the interface of the grid (i, j, k) and grid ($i + 1$, j, k). The transport coefficients at the other interfaces are also defined with similar formula.

Also, TPB density and pore diameter are evaluated in each grid. TPB is detected as the edge line among Ni, YSZ and pore voxels, and the sum of the length is measured in each grid. This method, however, overestimates the total TPB length because the actual TPB is expected to have much smoother shape. Therefore, we applied the scaling correction so that the total TPB length is the same as that obtained from the whole anode region by volume expansion method.[3] Pore diameter is evaluated by the line intercept method.[8,9] Lines are drawn in three directions along the orthogonal coordinate, whose origin is the focused voxel. The length of the lines intercepted by pore phase is measured and averaged to be used as the average pore diameter. We refer this model as SGS1 in the later sections.

SGS model 2: Interfacial connectivity.— For the further improvement of SGS model, it is required to consider the effect of the structural complexity on transport phenomena, especially when relatively coarse grid system is used. In macro-scale, this effect is generally evaluated

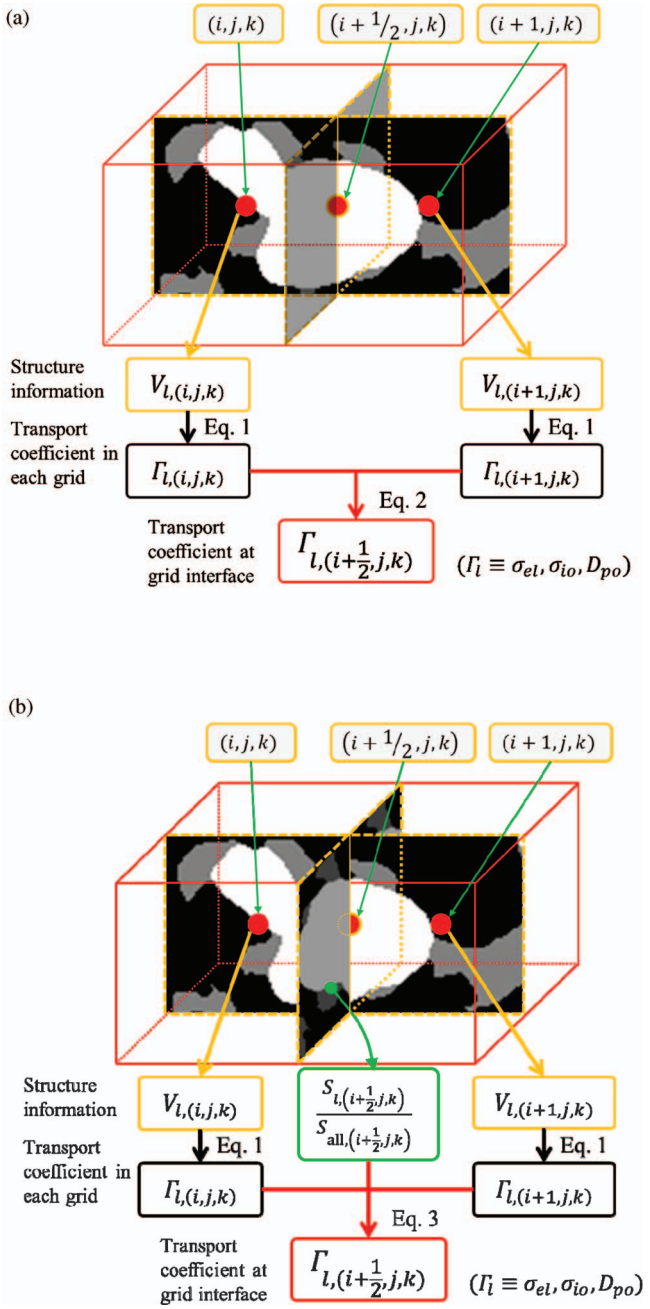

Figure 4. Schematic pictures of the sub-grid scale models proposed in this study. (a) SGS1, (b) SGS2.

by the tortuosity factor; however it is difficult and time-consuming to locally evaluate the tortuosity factor in every grid. For the development of a reliable SGS model, it is important to establish a simple and effective way to locally evaluate the structural complexity.

In the original image voxels, the structural complexity is elementarily ascribed to the connectivity of neighboring voxels. If the phases of two neighboring voxels are the same, they are connected and if not, the connectivity is zero. As a result of considering this on/off-type local connectivity for all voxels in the dataset, the macroscopic complexity is expressed. In the SGS model 2 (SGS2), we extend this expression of structural complexity to simulation grid. The difference is that because the simulation grid contains multiple image voxels, the connectivity of two neighboring grids are evaluated not by simple on/off-type connectivity but by considering the surface fraction of the conductive phase (Ni, YSZ or pore phase) on a grid interface. This is

considered as an attempt to evaluate the structural complexity by the surface information of the numerical grid. It is worth noting that the complexity expression using the surface information matches to the finite volume method, in which the transport of physical quantities between neighboring two grids is evaluated at the interface; hence evaluation of the effective transport coefficient on each interface is a key issue. By taking the grid connectivity into account, SGS2 is expected to better describe the effects of structural complexity on the transport phenomena than SGS1. The concept of the model is schematically illustrated in Fig. 4b. First, effective transport coefficient in each grid is evaluated with eq. 1, and then the value at the interface is evaluated by using the surface fractions of the conductive volume. Following formula shows the averaged effective transport coefficient at the interface between grid (i, j, k) and grid $(i + 1, j, k)$ as an example.

$$\Gamma^{eff}_{l,(i+\frac{1}{2},j,k)} = \frac{S_{l,(i+\frac{1}{2},j,k)}}{S_{all,(i+\frac{1}{2},j,k)}} \left(\frac{1}{\Gamma^{eff}_{l,(i,j,k)}} + \frac{1}{\Gamma^{eff}_{l,(i+1,j,k)}} \right)^{-1} \quad [3]$$

where S_{all} is the total surface area of the grid interface and S_l is the surface area of phase l on the grid interface. The transport coefficients at the other interfaces are also defined with similar formula.

Electron and ion transport.— In the SOFC anodes, electrons and oxygen ions are transported through the Ni phase and YSZ phase, respectively. Considering the conservation of these species, following equations are introduced as governing equations:

$$\nabla \cdot (\sigma^{eff}_{el} \nabla \phi_{el}) = -i_{tpb} \quad [4]$$

$$\nabla \cdot (\sigma^{eff}_{io} \nabla \phi_{io}) = i_{tpb} \quad [5]$$

where ϕ_{el} and ϕ_{io} are the electric potential in electron-conductive phase (Ni) and oxygen-ion-conductive phase (YSZ), respectively. i_{tpb} is the charge-transfer current exchanged between the two phases. $\sigma_{el}{}^{eff}$ and $\sigma_{io}{}^{eff}$ are effective electron/ion conductivities, which are evaluated depending on the applied SGS models. For bulk conductivities, σ_{el} and σ_{io}, we use following formulas[10,11]:

$$\sigma_{el} = 3.27 \times 10^6 - 1065.3T \quad [6]$$

$$\sigma_{io} = \left[2.94 \times 10^{-5} \exp\left(\frac{10350}{T} \right) \right]^{-1} \quad [7]$$

Diffusion of gas species.— Gaseous diffusion of hydrogen and steam is considered based on the dusty-gas model (DGM)[12,13]:

$$\frac{N_i}{D^{eff}_{i,K}} + \sum_{j \neq i} \frac{X_j N_i - X_i N_j}{D^{eff}_{ij}} = -\frac{P_t}{RT} \nabla X_i - \frac{X_i}{RT} \left(1 + \frac{K P_t}{\mu D^{eff}_{i,K}} \right) \nabla P_t \quad [8]$$

where X_i, N_i and P_i are molar fraction, molar flux and partial pressure of gas species i, respectively. P_t is the total pressure. $D_{i,K}{}^{eff}$ and $D_{ij}{}^{eff}$ are the effective Knudsen diffusion coefficient and the effective binary diffusion coefficient, which are evaluated depending on the applied SGS models. For the bulk binary diffusion coefficient, the Fuller-Schettler-Giddings' equation[14] is adopted in this study:

$$D_{ij} = \frac{0.01013 T^{1.75} \left(\frac{1}{M_i \times 10^3} + \frac{1}{M_j \times 10^3} \right)^{1/2}}{P[(\Sigma v_i \times 10^6)^{1/3} + (\Sigma v_j \times 10^6)^{1/3}]^2} \quad [9]$$

where M_i is the molecular mass, and Σv_i represents the diffusion volume of the molecule of species i.[15] The bulk Knudsen diffusion coefficient is estimated using the local pore diameter d_p as follows:

$$D_{i,K} = \frac{d_p}{2} \frac{2}{3} \sqrt{\frac{8RT}{\pi M_i}} \quad [10]$$

In the Eq. 8, the total pressure gradient term is neglected in this study. The total pressure is assumed to be almost constant over the whole anode region because the gas diffusion is significant inside the anode with relatively thin structure (30 μm) and large pore volume fraction (~50 %). In our previous 1D analysis,[5] we considered the total pressure gradient in the anode region; however, the difference in the pressure is almost negligible. Also 3D analysis using synthesized anode structure was conducted by Cai et al.[16] and little change in the pressure was obtained from their results. It should also be noted that we can significantly reduce the computation cost under the constant total pressure assumption.

Electrochemical reaction.— In SOFC anodes, electrochemical oxidation of hydrogen takes place at TPB. Currently the evaluation of the charge-transfer rate in SOFC electrodes is still an open issue. As R.J. Gorte et al. pointed out,[17] simple Butler-Volmer equation is not always valid in SOFC electrode because the equation is originally derived to describe reactions that take place at the surface of metal electrode in electrolytic solution. Therefore, many researches were devoted to investigate the charge-transfer rate in SOFC electrodes. Kawada et al.[18] experimentally investigated the charge-transfer rate with Ni-YSZ cermet anode in both anodic and cathodic regimes and developed a modified Butler-Volmer-like equation:

$$i_{tpb} = i_0 \left[\exp\left(\frac{2F}{RT} \eta_{act} \right) - \exp\left(-\frac{F}{RT} \eta_{act} \right) \right] \quad [11]$$

where i_0 is the exchange current density, and η_{act} is the activation overpotential. Although the physical meaning of the symmetric factor in Eq. 11 was not clarified, it might be attributed to the elementary electrochemical reaction at around the TPBs, such as H_2 adsorption and dissociation on Ni surface. Zhu et al.[19] assume that the adsorption/desorption of H_2 on Ni surface and H_2O on YSZ surface are at equilibrium, and derived another Butler-Volmer-like equation. Development of reliable charge-transfer model rooted from such elementary chemical reactions is indispensable for the precise numerical prediction of electrode performance.

In this study, we adopt the Eq. 11 for the charge-transfer model because the model was also used in the 3D numerical analysis by Shikazono et al.[6], in which the same anode structure data obtained by FIB-SEM was used. Therefore, it becomes easier to compare our results with theirs so that we can check the validity of the numerical model proposed in this study.

Activation overpotential is defined as follows:

$$\eta_{act} = \phi_{el} - \phi_{io} - \eta_{con} \quad [12]$$

where η_{con} is the concentration overpotential expressed as follows:

$$\eta_{con} = \frac{RT}{2F} \ln \left(\frac{P_{H_2,bulk}}{P_{H_2}} \frac{P_{H_2O}}{P_{H_2O,bulk}} \right) \quad [13]$$

where $P_{H_2,bulk}$ and $P_{H_2O,bulk}$ are the gas partial pressures on the anode surface. The exchange current density i_0 in the Eq. 11 is assumed to have a linear dependency on the TPB density l_{tpb}:

$$i_0 = i_{0,tpb} l_{tpb} \quad [14]$$

where $i_{0,tpb}$ is the exchange current per unit TPB length. We use an empirical relationship for the $i_{0,tpb}$ [20,21]:

$$i_{0,tpb} = 31.4 P^{-0.03}_{H_2} P^{0.4}_{H_2O} \exp\left(-\frac{18300}{T} \right) \quad [15]$$

Boundary conditions.— Boundary conditions used in the anode overpotential analysis are summarized in Table I. Gas compositions

Table I. Boundary Conditions.

Variables	Surface ($z = 0$)	Interface ($z = L$)
H_2 Partial Pressure	$P_{H_2}(0) = P_{H_2,bulk}$	$\frac{dP_{H_2}}{dx}(L) = 0$
H_2O Partial Pressure	$P_{H_2O}(0) = P_{H_2O,bulk}$	$\frac{dP_{H_2O}}{dx}(L) = 0$
Electric Potential in Ni	$\phi_{el}(0) = \eta_t$	$\frac{d\phi_{el}}{dx}(L) = 0$
Electric Potential in YSZ	$\frac{d\phi_{io}}{dx}(0) = 0$	$\phi_{io}(L) = 0$

are constant on the anode surface to represent the supplied fuel composition. To determine the anode overpotential, the electric potential in the Ni phase at the anode surface and that in the YSZ phase at the anode-electrolyte interface are properly set.

Results and Discussion

Global microstructural parameters.— Prior to the numerical simulation, microstructural parameters, such as volume fraction, tortuosity factor, surface-to-volume ratio and TPB density, are quantified in the whole sample volume as "global" microstructural parameters. The results have been already reported in our previous works,[3,5,22] therefore, we just summarize the sample sizes and voxel sizes in Table II, and the quantified global microstructural parameters in Table III. Tortuosity factor is quantified by the random-walk-based diffusion simulation[5] and TPB density by the volume-expansion method.[3]

Grid system.— Table IV summarizes the information of the grid systems used in the numerical analysis. The effect of the grid size can be clearly presented by Fig. 5 that shows the distributions of the Ni volume fraction in Grid 1 and Grid 4. The grid size of Grid 1 is about 1 μm and comparable to the characteristic scale of the original porous structure. As shown in Fig. 5a, Grid 1 no more keeps the details of the original structure. On the other hand, Grid 4 reasonably keeps the original structure (Fig. 5b). The portion of grids containing more than two phases is small but they naturally exist at important locations: the boundaries of different two phases, and TPB. Note that the grid size of Grid 4 is almost the same as that used in the 3D simulation by Shikazono.[6]

To show one aspect of the relation between the grid and the original microstructure, the volume fractions are evaluated in each grid and shown as histograms in Fig. 6. When the volume fraction, V, is unity, the grid is fully occupied by the phase of interest. When the phase of interest is not included in the grid, the volume fraction is zero. In the extreme case where the original image voxel is used as the calculation grid, V is either unity or zero in every grid. As shown in Table IV, the grids used in the present calculation are always larger than the original image voxel. As the grid size becomes larger, two or more phases tend to be included in one grid and the portion of $V = 0$ or 1 decreases. Moreover, in the case of Grid 1, which is the coarsest grid in this study, the distributions seem to have peaks, and the peak values are close to the values of global microstructural parameters shown in Table III. The proposed SGS models are required to exert their effect especially in coarser grid cases, where one grid includes two or more phases.

Table II. Observed Size and Voxel Size of Anode Sample.

	Unit	X	Y	Z
Observed Size	[μm]	19.2	8.51	6.20
Voxel Size	[nm]	26.6	26.6	62.0
Number of Voxel		720	320	100

Table III. Global Microstructural Parameters.[5]

		Unit	Ni	YSZ	Pore
Volume fraction		[%]	25.3	25.1	49.6
Tortuosity factor	X		25.2	24.0	1.95
	Y		34.8	13.4	1.97
	Z		6.91	8.85	1.74
Surface-to-volume ratio		[$\mu m^2/\mu m^3$]	3.56	7.51	4.12
TPB density		[$\mu m/\mu m^3$]		2.49	

Diffusion simulation.— To confirm the validity of the proposed SGS models, we conduct a simple diffusion simulation prior to the anode overpotential analysis. We set the potential difference at the both edge sections perpendicular to the Z direction and induce flux through the calculation domain. From the amount of the induced flux, the effective transport coefficient of phase l, Γ_l^{eff} is obtained in the overall calculation domain, and subsequently the tortuosity factor of the phase, τ_l, is obtained as follows:

$$\tau_l = V_l \frac{\Gamma_l}{\Gamma_l^{eff}} \quad [16]$$

If the obtained tortuosity factor is the same as the global microstructural parameter obtained by the random-walk simulation (Table III), we can judge that the calculation domain reasonably keeps the original structural complexity of the porous anode. If the size of the grid is small enough, we can expect the calculation domain itself naturally represents the structural complexity. In contrast, if it is not, the structural complexity may be underestimated.

The calculated tortuosity factors in the Grid 1–4 with SGS1 and SGS2 are shown in Fig. 7. In these figures, tortuosity factors obtained by the diffusion simulation are normalized by those obtained by random-walk simulation. As expected, with the SGS1, the value of τ_{SGS}/τ_{RW} approaches to unity (dotted line) as the grid becomes finer. However, the values are still below unity because the information of structural inhomogeneity inside the grid is inevitably lost. Such tendency is prominent especially in the YSZ phase because of the small characteristic scale of the phase, which is indicated by the large surface-to-volume ratio as shown in Table III. If the characteristic scale of a phase is smaller, much finer grid system is necessary to precisely capture the structure.

By correcting the transport flux with the SGS2, the trend in the figures is drastically changed; the amount of flux is modified to make the values of τ_{SGS}/τ_{RW} approach to unity. However, there is a difference in trend among the phases. In the Ni and YSZ phases, tortuosity factors are reasonably evaluated even in the coarser grid, which is a remarkable improvement by applying the SGS model. Even though there is a small overshoot in the Grid 3, the values tend to converge to the dotted lines. It can be said that the SGS2 effectively improves the evaluation of the transport flux especially in coarser grids, which is one of the most important aspect required for SGS models. In the pore phase, however, tortuosity factor is overestimated in the coarser grids, which indicates the flux modification is stronger than required. Although the different tendency may be attributed to the structural difference between the pore and the solid phases, the reason is not

Table IV. Grid System Information.

	Grid Size [μm]			Number of Grid		
	X	Y	Z	X	Y	Z
Grid 1	1.06	1.06	1.24	18	8	5*5
Grid 2	0.532	0.532	0.620	36	16	10*5
Grid 3	0.266	0.266	0.310	72	32	20*5
Grid 4	0.133	0.133	0.124	144	64	50*5

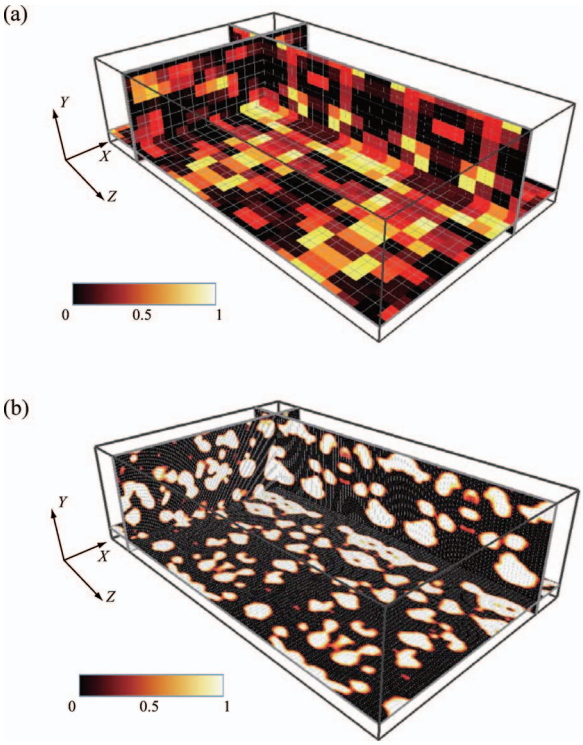

Figure 5. Distribution of the Ni volume fraction. (a) Grid 1. (b) Grid 4.

fully clear so far. Considering that the SGS models applied in this study are simple and still in their early stage of development, it leaves a possibility of further improvement of the SGS models by considering the structure inside the grid.

From the above results that the structural complexity is still underestimated in the fine grid (Grid4) with the SGS1, it is easy to infer that the conventional resampling approach, in which a grid is replaced with the phase of the largest volume fraction in the grid, induces severe deterioration of structural information. Use of an appropriate SGS model is recommended when resampling process is involved in grid generation. The SGS2 proposed in this study is one of the examples for the solution.

Anode overpotential analysis.— Numerical simulation to predict the anode polarization characteristics is conducted with the proposed SGS models. Calculation parameters are summarized in Table V. Total gas pressure and anode temperature are assumed to be constant and uniform, and supplied fuel is 3 % humidified hydrogen. Anode overpotential is set as a boundary condition and the average current density is obtained as a simulation result. Figure 8 shows the result obtained with each SGS model. With the SGS1, polarization curves strongly depend on the grid sizes (Fig. 8a), while little dependency is found with the SGS2 (Fig. 8b). In spite of the variations of the evaluated tortuosity factors (Fig. 7), overpotential characteristics are less sensitive to the variation in the SGS2 case. This is consistent with the findings in our previous report;[22] we conducted a sensitivity analysis to investigate the effect of microstructural parameters on the performance and found that the YSZ tortuosity factor had the largest influence. Its effect on the performance is non-linear and becomes prominent when the YSZ tortuosity factor is smaller than about 5. As shown in Fig. 7, the YSZ tortuosity factor is relatively high for the present microstructure and the estimation by the SGS2 agree fairly well. This is the reason why the overpotential characteristics are almost the same in the SGS2 cases and match well with the experiment.

The distribution of the average charge-transfer current in the thickness direction of the anode is shown in Fig. 9. Calculation parameters

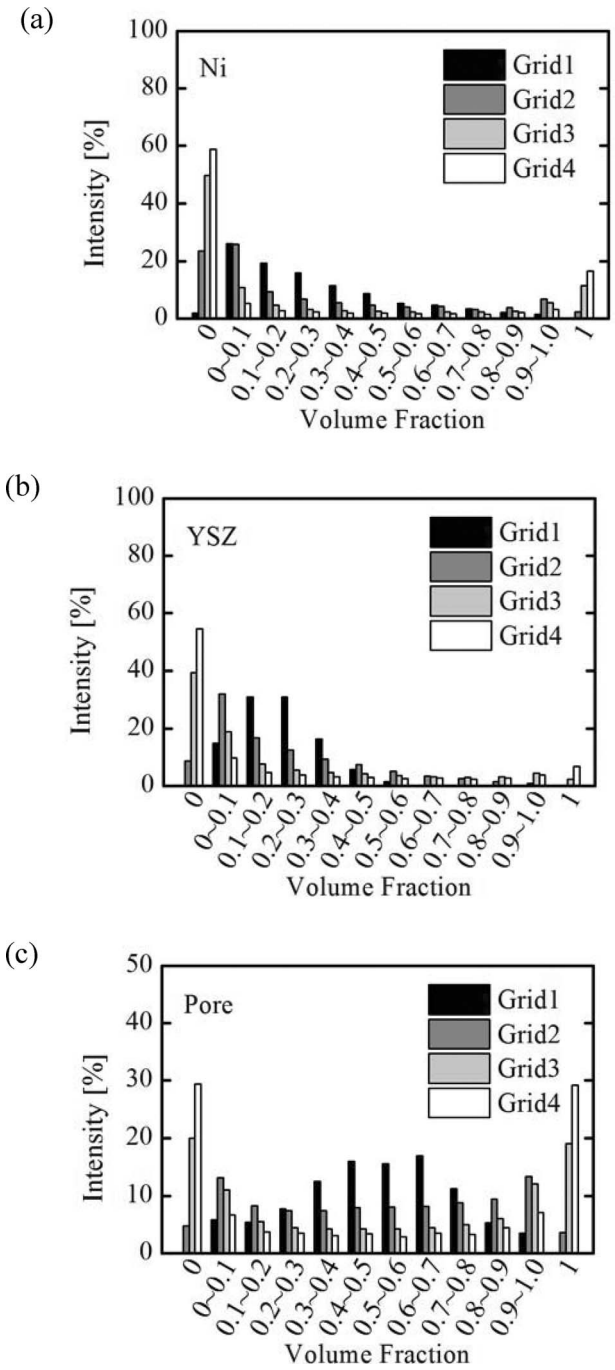

Figure 6. Histograms of the volume fractions. (a) Ni, (b) YSZ, (c) Pore.

shown in Table V are used, and anode overpotential is set 0.05 V. Charge-transfer current calculated locally with Butler-Volmer equation (eq. 11) is averaged over the *X-Y* plane which is perpendicular to the thickness direction of the anode, *Z*. As clearly shown in Fig. 9a, the distributions vary depending on the grid size when SGS1 is applied. On the other hand, little dependency is found for SGS2 (Fig. 9b). The electrochemically active region in the case of SGS2 is within about 10 μm from the anode-electrolyte interface, which is consistent with our previous 1D approach[5] and experimental reports by other researchers.[23,24] These results support the effectiveness of the SGS2 to capture the structural complexity of the calculation domain. The overpotential characteristics and reaction current distribution are all represented properly even under a relatively coarse grid.

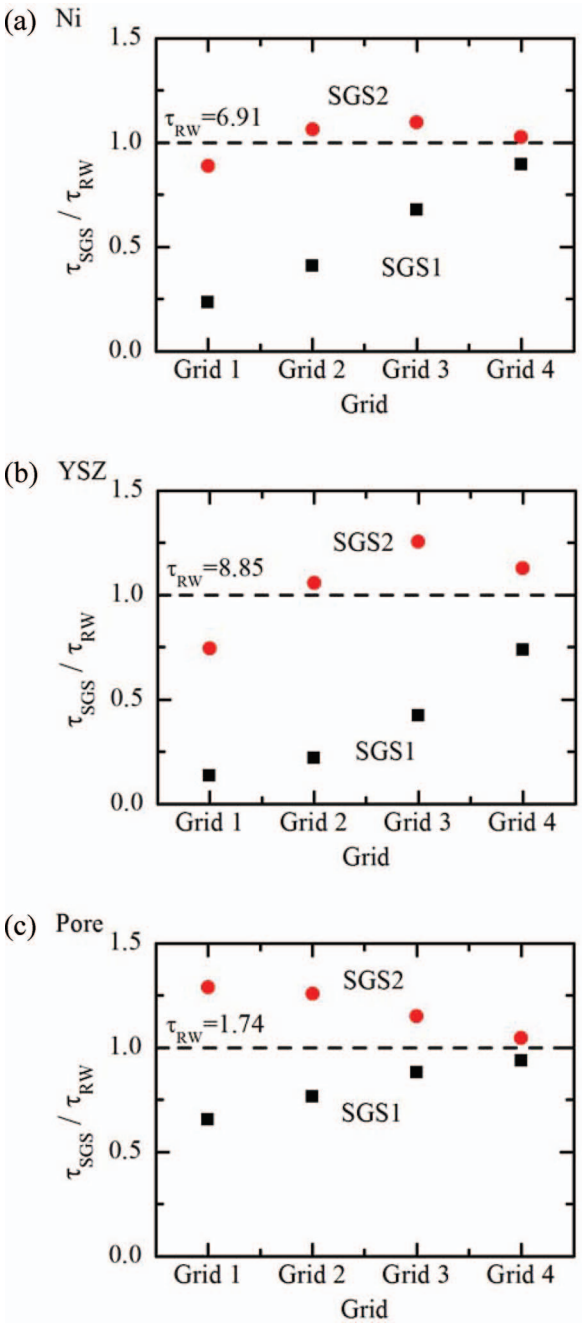

Figure 7. Tortuosity factors obtained by the diffusion simulation. (a) Ni (b) YSZ, (c) Pore. The values are normalized by the tortuosity factors obtained by random-walk simulation.

Figure 10 shows the comparison of overpotential characteristics between experiment and simulation. For the simulation result, 3D numerical analysis with LBM by Shikazono et al.[6] is also shown in addition to our FVM-based analysis, where Grid4 with SGS2 is applied. The anode examined under the condition of 1.2 % and 10 % humidified hydrogen at 1000°C was provided for the FIB-SEM observation, and obtained structural data was shared among our group and Shikazono's group. Electrochemical characterization at 3.0 % humidified condition was also conducted with the anode fabricated through completely the same process as the observed anode. These two anodes can be assumed to have the same porous structure. First, comparing the results obtained by the two different simulation methods, FVM with SGS model gives slightly lower performance in all the fuel conditions. This result is reasonable because in the FVM analysis with the SGS model, the structural complexity inside the grid is considered; hence the effective transport coefficients become slightly lower. Note that the grid sizes used in both simulations are almost the same (about 120 nm). Next, comparing the results obtained by experiment and simulation, the overpotential characteristics at relatively low humidified conditions: 1.2 % and 3.0 %, are quantitatively reproduced by the simulation. On the other hand, in the relatively high humidified condition, the anode overpotential is about twice overestimated. Similar tendencies are also obtained in our previous 1D analysis.[5] These discrepancies between experiment and simulation can mostly be attributed to the charge-transfer model adopted in this study, where the electrochemical oxidation of hydrogen is assumed to be an overall reaction. To capture the realistic process at the TPB, the elementary chemical reactions on the catalytic surface should be considered with the aid of surface coverage of adsorbed chemical species. The development of more sophisticated charge-transfer model is required for reliable simulation.

From the above discussion, the overall anode model has more to be improved particularly around the evaluation of the charge-transfer

Table V. Calculation Parameters.

	Symbol	Value	Unit
Total pressure	P_t	1.013×10^5	[Pa]
Temperature	T	1273	[K]
H_2 partial pressure	$P_{H_2,bulk}$	$0.97 \times P_t$	[Pa]
H_2O partial pressure	$P_{H_2O,bulk}$	$0.03 \times P_t$	[Pa]
Anode thickness	L	31.0	[μm]
Anode overpotential	η_t	0.01∼0.05	[V]

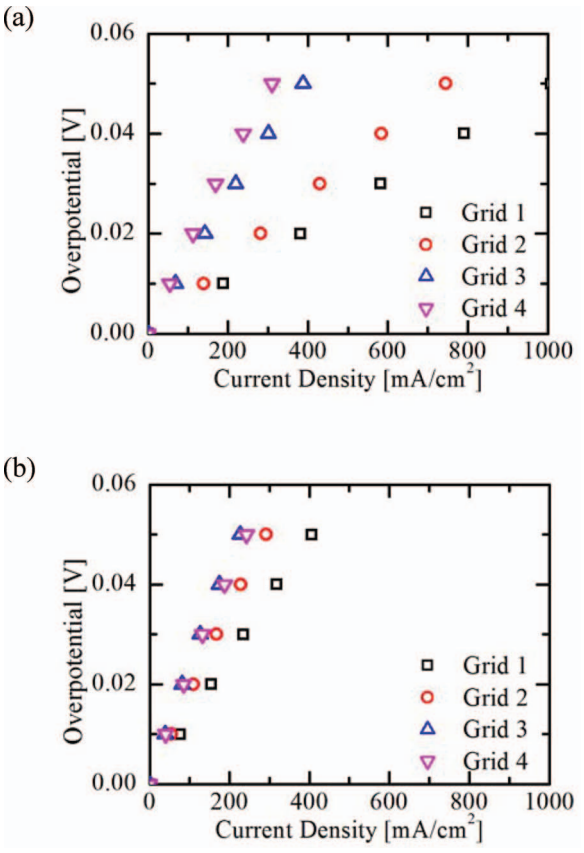

Figure 8. Anode overpotentials. (a) SGS1. (b) SGS2.

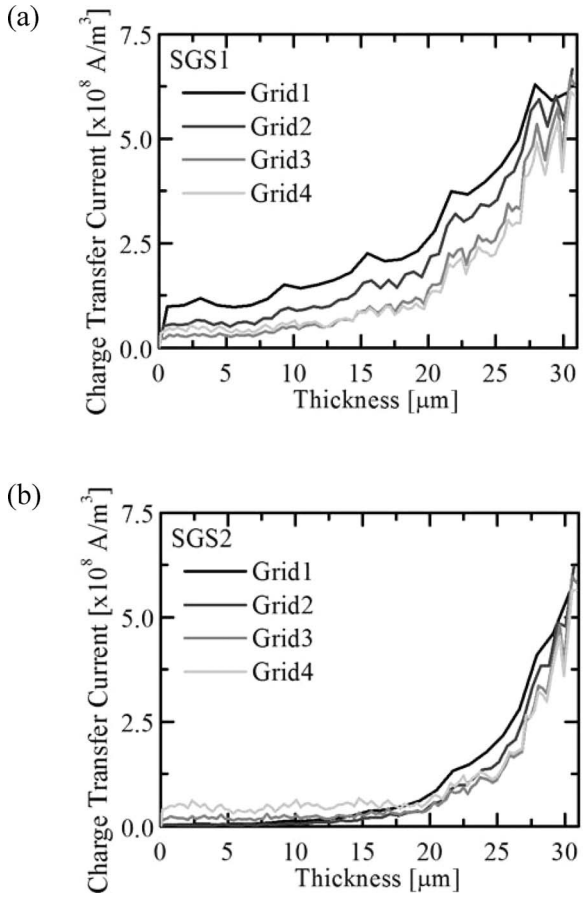

Figure 9. Distribution of the averaged charge-transfer current. (a) SGS1. (b) SGS2. Anode overpotential is 0.05 V.

rate. However, it should be stressed that the main contribution of this paper is to develop the SGS model, with which we can keep the quality of the structural information obtained by FIB-SEM in the grid system. The validation of the SGS model itself is successfully done by the comparison of tortuosity factor in the previous section.

Computation time.— Computation time required to obtain a convergent solution is shown in Fig. 11. Since it slightly varies according to the applied SGS models and boundary conditions, the average computation times are shown. In each calculation, we use a single core of Core 2 Duo E8600 processor. The time required in the Grid 2 is more than 200 times less than that in the Grid 4. It clearly shows the effectiveness of the proposed SGS model. If coarser grid can be

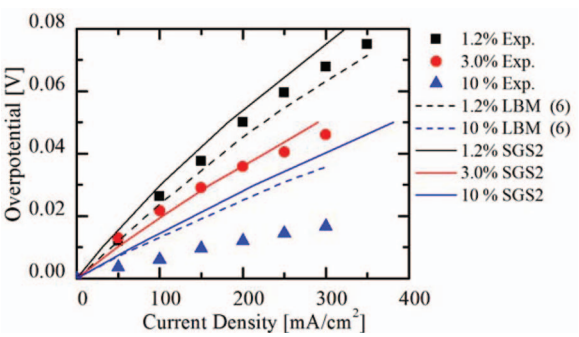

Figure 10. Comparison of the overpotential analysis between experiment and numerical simulation.

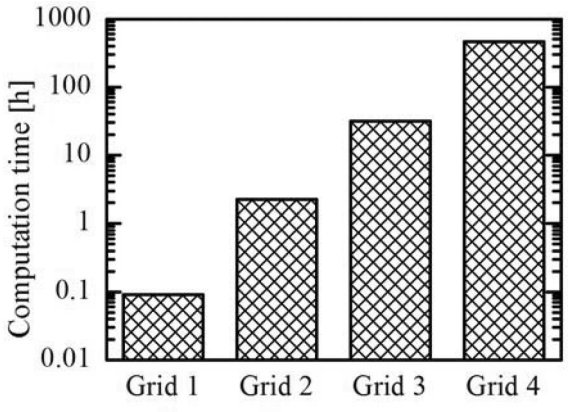

Figure 11. Computation time required to obtain convergent solution.

used in the electrode simulation without losing accuracy, an electrode simulation can be applied to much wider-scale analysis. We believe the proposed SGS model has a potential to act as a bridge builder between micro-scale analysis and macro-scale analysis.

Conclusions

Three-dimensional simulation to predict the SOFC anode polarization is performed with a structure obtained by FIB-SEM. A sub-grid scale model (SGS) is newly developed and effectively used to improve the quality of the structural information after resampling process. By considering the phase connectivity between the neighboring grids, structural complexity of the porous anode is reasonably taken into account. As a result, transport flux through the porous anode is properly evaluated, and anode polarization characteristics are reasonably predicted even when coarser grid system is used. The proposed SGS model shows its potential for two aspects: reducing computational load and improving simulation accuracy. It can reduce the computation cost and time without losing simulation accuracy even when coarser grid is used. Therefore, the SGS model may be an effective tool to combine electrode simulation with much larger-scale analysis, such as cell-scale analysis. In addition, if we use the fine grid with appropriate SGS model, the simulation accuracy is definitely better than the conventional approach, in which grid phase is replaced by the phase of the largest volume fraction in the grid. It is recommended that an appropriate SGS model is applied to the numerical simulation of SOFC porous electrodes based on a 3D microstructure dataset when the resampling process is necessary. The SGS models proposed in this study are found to be effective but further improvement should be possible and needed to bridge the micro-scale and macro-scale simulations.

Acknowledgments

This work was supported by the New Energy and Industrial Technology Development Organization (NEDO) under the Development of System and Elemental Technology on Solid Oxide Fuel Cell (SOFC) Project.

References

1. J. R. Wilson, W. Kobsiriphat, R. Mendoza, H.-Y. Chen, J. M. Hiller, D. J. Miller, K. Thornton, P. W. Voorhees, S. B. Adler, and S. A. Barnett, *Nature Material*, **5**(7), 541 (2006).
2. P. R. Shearing, J. Golbert, R. J. Chater, and N. P. Brandon, *Chemical Engineering Science*, **64**(17), 3928 (2009).
3. H. Iwai, N. Shikazono, T. Matsui, H. Teshima, M. Kishimoto, R. Kishida, D. Hayashi, K. Matsuzaki, D. Kanno, M. Saito, H. Muroyama, K. Eguchi, N. Kasagi, and H. Yoshida, *Journal of Power Sources*, **195**, 955 (2010).
4. D. Gostovic, J. R. Smith, D. P. Kundinger, K. S. Jones, and E. D. Wachsman, *Electrochemical and Solid-State Letters*, **10**(12), B214 (2007).

5. M. Kishimoto, H. Iwai, M. Saito, and H. Yoshida, *Journal of Power Sources*, **196**, 4555 (2011).
6. N. Shikazono, D. Kanno, K. Matsuzaki, H. Teshima, S. Sumino, and N. Kasagi, *Journal of The Electrochemical Society*, **157**(5), B665 (2010).
7. P. R. Shearing, Q. Cai, J. I. Golbert, V. Yufit, C. S. Adjiman, and N. P. Brandon, *Journal of Power Sources*, **195**, 4804 (2010).
8. D. Simwonis, F. Tietz, and D. Stöver, *Solid State Ionics*, **132**, 241 (2000).
9. J.-H. Lee, H. Moon, H.-W. Lee, J. Kim, J.-D. Kim, and K.-H. Yoon, *Solid State Ionics*, **148**, 15 (2002).
10. U. Anselmi-Tamburini, G. Chiodelli, M. Arimondi, F. Maglia, G. Spinolo, and Z. A. Munir, *Solid State Ionics*, **110**, 35 (1998).
11. N. F. Bessette II, W. J. Wepfer, and J. Winnick, *Journal of The Electrochemical Society*, **142**(11), 3792 (1995).
12. E. A. Mason, A. P. Malinauskas, and R. B. Evans III, *The Journal of Chemical Physics*, **46**(8), 3199 (1967).
13. D. Aronšt and P. Schneider, *The Chemical Engineering Journal*, **57**, 91 (1995).
14. E. N. Fuller, P. D. Schettler, and J. C. Giddings, *Industrial and Engineering Chemistry Research*, **58**(5), 18 (1966).
15. R. H. Perry, *Perry's Chemical Engineers' Handbook 7th Edition*, McGraw-Hill, New York (1981).
16. Q. Cai, C. S. Adjiman, and N. P. Brandon, *Electrochimica Acta*, **56**, 10809 (2011).
17. R. J. Gorte and J. M. Vohs, *Annual Review of Chemical and Biomolecular Engineering*, **2**, 9 (2011).
18. T. Kawada, N. Sakai, H. Yokokawa, M. Dokiya, M. Mori, and T. Iwata, *Journal of The Electrochemical Society*, **137**(10), 3042 (1990).
19. H. Zhu, R. J. Kee, V. M. Janardhanan, O. Deutschmann, and D. G. Goodwin, *Journal of The Electrochemical Society*, **152**(12), A2427 (2005).
20. B. De Boer, Ph.D. thesis, University of Twente, The Netherland (1998).
21. Y. Suzue, N. Shikazono, and N. Kasagi, *Journal of Power Sources*, **184**, 52 (2008).
22. M. Kishimoto, H. Iwai, M. Saito, and H. Yoshida, *Proceedings of the 14th International Heat Transfer Conference*, IHTC14-22495, **37** (2010).
23. S. Primdahl and M. Mogensen, *Journal of the Electrochemical Society*, **144**(10), 3409 (1997).
24. M. Brown, S. Primdahl, and M. Mogensen, *Journal of The Electrochemical Society*, **147**(2), 475 (2000).